Acta Cryst. (1966). **21**, 103

Theory of the Measurement of Integrated Intensities Obtained with Single-Crystal Counter Diffractometers*

BY J. LADELL AND N. SPIELBERG

Philips Laboratories, Briarcliff Manor, New York, U.S.A.

(*Received* 23 *June* 1965)

A comprehensive analysis of reflected intensity profiles generated by single-crystal diffractometric methods has been carried out. The observed profile $U_0(\beta)$ is the multiple convolution of six component distributions: the intrinsic diffraction pattern or interference function, the source intensity distribution, the angle scale spectral distribution, the crystal size distribution, the crystal imperfection due to lattice distortion or strain, and the angular distribution of crystal blocks in the mosaic. Whenever the entire profile is generated by rotating the crystal at constant angular velocity through a range in excess of the range for which the multiple convolution has appreciable value, and when all the generated intensity is detected by either a stationary or moving detector which subtends an adequate aperture, the quantity measured, $\int_{-\infty}^{\infty} U_0(\beta)\,d\beta$, is proportional to the integral of the intrinsic diffraction pattern at all 2θ angles. The constant of proportionality is the product of the integrals of the remaining components. Alleged differences between 'ω' and '2:1' scans are due to failure to produce or to detect the entire profile.

The experimental feasibility of isolating neighboring reflections depends upon the unit-cell size and the ranges of the component distributions. Because of the large inherent ranges of some of the component profiles, the production and detection of the entire resolved diffraction intensity is not always feasible. When crystal monochromators are not used, an evaluation of the systematic errors is intractable. The control of experimental parameters, particularly the spectral band pass, through crystal monochromatization, however, reduces or eliminates systematic errors due to the truncated rotation of the study crystal and limited detector aperture. By considering the mechanism of intensity profile generation, a formalism has been developed by means of which the systematic error for a given set of experimental parameters can be theoretically predicted.

Introduction

The application of modern techniques has made possible the rapid and automatic collection of large quantities of single-crystal X-ray diffraction data of high precision. At the same time, the advent of large capacity, high-speed digital computers makes possible the manipulation and refinement of large masses of data to yield crystallographic data of great detail and complexity. Inevitably, however, it has been realized that the full power of modern techniques cannot be achieved without a thorough understanding of the various factors entering into X-ray intensity measurements. Studies of integrated intensity measurements on the basis of convolution theory have been reported recently by Alexander & Smith (1962, 1964) and Burbank (1965). Their work has been limited to the case of non-monochromatized incident radiation, but makes use of a spectral model more appropriate to the case of monochromatized radiation, presumably for the sake of mathematical convenience. Moreover, an adequate account of the effect of the 'background' on intensity measurements has not been presented in the literature.

In this paper we outline the theory of single-crystal intensity measurement with the use of monochromatized radiation and the effect of some experimental conditions on possible systematic errors.

Convolution theory

An elementary consequence of convolution theory is that the area under an observed profile is the product of the areas under the individual component profiles which convolute to form the observed profile. Ideally, in structure analysis, one would like to measure the intrinsic diffraction pattern. The area under this diffraction pattern is the theoretical integrated intensity from which the structure factor can be deduced. It is experimentally impossible to measure this diffraction pattern directly since the experimental conditions required are strictly monochromatic parallel radiation and a perfect monocrystal. In a realistic experiment in which polychromatic divergent radiation is used in conjunction with real crystals which exhibit mosaic spread, *etc.*, departures from the ideal give rise to what may be considered 'smearing' aberrations. These distort the intrinsic diffraction pattern, yielding as an observed profile a multiple convolution of the intrinsic diffraction pattern and the smearing aberrational dis-

* Preliminary account presented at Sixth Congress of I.U.Cr., Rome, Italy (1963), Acta Cryst. **16**, A148.

tributions. Since the area under the observed profile is the product of the areas under the component profiles, a relative measure of the area of the intrinsic diffraction pattern for each reflection is available from a realistic experiment, provided that the integral of the entire observable profile of each reflection is measured; the product of the areas of each of the smearing aberrations will then constitute a constant scale factor*. Failure to measure the integral of the entire developable profile for a given reflection will give rise to an error in the determined F^2. Because the observed profile is expanded in a complicated way with increasing 2θ angle owing to the dispersive nature of one or more of the component profiles, it is not likely that the same percentage error will be made in failing to integrate completely profiles occurring at different 2θ angles. Accordingly, for any technique of measurement in which only part of the integral of the entire profile is measured, determined structure factors will be subject to a systematic error. In general, for both the 2:1 and ω scan techniques, the systematic error (as a function of 2θ) will cause an underestimation of F^2 at high 2θ angles, and this would be revealed in electron density distributions as spurious contributions to the thermal vibration parameters and possibly incorrect atomic locations. In any event, knowledge of the existence of a systematic error is enough to invalidate conclusions as to the accuracy of a structure determination which are based solely on random error statistics. The important significance of the convolution theorem is not only that it provides a formalism by means of which systematic error can be studied, but also that it permits an exact definition of integrated intensities which is consistent both with theory and with experimental observables.

To investigate the sources of possible systematic error in the measurement of integrated intensities, we must enumerate and investigate the nature of the component profiles and determine on the basis of a knowledge of the component profiles to what extent the measurement of the integral of the entire observable profile is feasible. Experimentally, control may be exercised over some of the component profiles to reduce or eliminate the sources of systematic error. Also, the technique of measurement can be optimized to minimize residual systematic error where present. The question of optimization, however, (*e.g.* whether the ω scan or 2:1 tracking technique is more satisfactory) is a secondary consideration, since this practical question comes into focus only after experimental ingenuity has been exhausted in reducing the aberrational components. It may be easily inferred from the works of Furnas (1957), Alexander & Smith (1962, 1964), Burbank (1964) and Ladell & Spielberg (1963) that the requisite minimum receiving apertures required for both the ω and 2:1 scan techniques are governed by the effective ranges of the component profiles. When the minimum apertures are realistically maintained, the only practical difference (on the basis of which one technique can be preferred over the other) is that the technique requiring the larger aperture conceivably may involve a less favorable signal-to-noise ratio. On the other hand, where requisite minimum receiving apertures are not employed, or are unfeasible, and apertures smaller than the required 'minimum' apertures are used, there will be superimposed upon the systematic error of failing to generate the entire profile another source of systematic error: that of failing to detect portions of the generated profile.

We use a condensed notation to characterize the observed profile. Let β measure angular deviation of the study crystal from Bragg angle. Then $U_0(\beta)$, the observable profile, is given by

$$U_0(\beta) = U_1 * U_2 * U_3 * U_4 * U_5 * U_6(\beta) \qquad (1)$$

for the case of nonmonochromatized incident radiation. $U_1(\beta)$ is the intrinsic diffraction pattern involving the structure factor F, $U_2(\beta)$ is the source intensity distribution, $U_3(\beta)$ is the angle scale spectral distribution, $U_4(\beta)$ is the crystal size and shape distribution, $U_5(\beta)$ is the radial mosaic spread component or distribution-in-d (Ladell, 1961), and $U_6(\beta)$ is the transverse (angular mosaic spread) distribution. A summary of these distributions and the aperture contributions they imply is shown in Table 1. We distinguish between dispersive and nondispersive components (as do Alexander & Smith) reserving odd indices for dispersive components. Also, we specify the range in β over which each of these distributions exists by subscripting β. Thus, $U_i(\beta)$ is nonzero in the range $(-\beta_i, \beta_i)$.

Alexander & Smith (1962, 1964) have discussed the distributions $U_2(\beta)$, $U_3(\beta)$, $U_4(\beta)$ and $U_6(\beta)$, and have formulated a reasonable procedure for attacking the problem. Unfortunately, for the sake of mathematical convenience they were apparently forced to adopt a spectral model $U_3(\beta)$ which is so different from the actual conditions of experiment (particularly when Mo or Ag K radiation is used) as grossly to vitiate their analysis. On the other hand, were more realistic models adopted, both for the spectral and other components, the analysis would prove intractable in the case of β-filtered radiation. In succeeding sections of this paper we will discuss experimental conditions under which a physically realistic and mathematically tractable spectral model can be obtained.

Similarly, the assumption of a Gaussian model for $U_6(\beta)$ has serious consequences on the correct elucidation of both the physical aspects of crystal imperfection and the implied extent of minimum receiving apertures. This is true because in order to make sound and effective use of a theory based upon convolutions in the significant interpretation of single-crystal diffractometric profiles, one must take adequate account of the infinite ranges of some of the component profiles. A consequence of convolution theory is that if

* The scale factor is constant after correction for the Lorentz and other geometric factors.

each of the component distributions $U_i(\beta)$ is nonzero in the range $(-\beta_i, \beta_i)$ then the range of $U_0(\beta)$, $(-\beta_0, \beta_0)$, is such that

$$2\beta_0 = 2\sum_{i=1}^{6}\beta_i \,. \qquad (2)$$

While equation (2) is strictly valid in defining the range over which $U_0(\beta)$ has nonzero value, it should be emphasized that β_0 is infinite if any of the β_i's are infinite. Some of the distributions are indeed of infinite range. It becomes necessary in practice to truncate these distributions by replacing true ranges with effective ranges. When, however, infinite ranges are replaced by effective ranges, equation (2) does not retain its validity for indicating the effective range $2\beta_0$ as equal to $2\Sigma\beta_i$. Thus, for example, if it is stipulated that, for a distribution $U_i(\beta)$ monotonically decreasing towards $+\beta$ and $-\beta$, we define the effective range as that which includes the portion of the profile between abscissae for which the corresponding ordinates on both sides of the profile have fallen to 0·1% of peak value, it will be fortuitous if the effective range of the observed profile $U_0(\beta)$, similarly defined, is equal to the sum of the effective ranges of the component distributions. As a consequence, one cannot deduce the effective ranges of the component distributions. As a consequence, one cannot deduce the effective range of an individual component distribution by subtracting from the observed effective range of the observed profile the presumably known ranges of the other component distributions.

In applying convolution theory to observed profiles, particularly where high backgrounds are encountered, one must be careful to distinguish between coherently scattered radiation and incoherently scattered radiation. The nature of coherently scattered radiation, whether due to a characteristic line or white radiation, is such that its presence in the observed profile is not restricted to the base of the profile. Accordingly, neglect of the apparent background in horizontal truncation procedures introduces a source of systematic error unless the apparent background is virtually all incoherent scatter. On the other hand, if the background contains a mixture of coherent and incoherent radiation in significant proportions, inclusion of background also introduces an error due to the unknown incoherent portion. Thus, to avoid indeterminate systematic error in treating the background, experimental conditions should be chosen so as effectively to diminish sources of background.

Table 1. *Component distributions*

Symbol	Description	Model	Remarks	Requisite contribution to receiving aperture	
				ω scan	2:1
$U_1(\beta)$	Intrinsic diffraction profile			$4\beta_1$	0
	1. Small mosaic	$F^2 \exp(-K\beta^2)$	Delta function		
	2. Large mosaic	Laue term $= \frac{G(F)}{1+K\beta^2}$	$F<G(F)<(F^2)$ α displacement due to refraction		
		Bragg term $= \frac{G(F)\,H(\beta)}{1+K(\beta-\alpha)^2}$			
	3. Real crystal	Mixture of (1) and (2)			
$U_2(\beta)$	Source distribution	$1-\frac{1}{2}\cosh\frac{1{\cdot}3\beta}{\beta_2}$ $\lvert\beta\rvert<\lvert\beta_2\rvert$ O elsewhere	Real case probably asymmetric	$2\beta_2$	$2\beta_2$
$U_3(\beta)$	Angle scale spectral distribution				
	1. Filtered	Fig. 1(*b*)	'Infinite' range	$4\beta_3$	0
	2. Monochromatized	Fig. 1(*c*)	Truncated Cauchy		
$U_4(\beta)$	Crystal size (sphere)	$\sin^2\beta_4-\sin^2\beta$ $\lvert\beta\rvert\leq\lvert\beta_4\rvert$ 0 elsewhere	Vertical divergence assumed negligible	$4\beta_4\cos\theta$	$4\beta_4\cos\theta$
$U_5(\beta)$	Radial mosaic disorder	Distribution in d spacing	Probably anisotropic	$4\beta_5$	0
$U_6(\beta)$	Normal mosaic angular distribution	Usually assumed Gaussian Possibly Cauchy distribution	Effective range large if Cauchy	0	$4\beta_6$

Description of component distributions

The distribution $U_1(\beta)$, the intrinsic diffraction pattern according to the dynamical theory for a perfect single crystal with a spherical boundary, has not been worked out in detail. Depending upon the 2θ angle, the distribution should be some weighted average of the Bragg and Laue diffraction patterns (Zachariasen, 1945). The distribution $U_1(\beta)$ should be extremely narrow, having a line width (full width at half maximum) of a few seconds of arc at small 2θ angles. The Bragg term should cause a small displacement of $U_1(\beta)$ from the calculated $2\theta_0$ position (corresponding to the d spacing and wavelength λ_0) owing to refraction; the distribution should be asymmetric at high 2θ angles where the Bragg term predominates and should be more symmetric at low angles where the Laue term predominates. The decay of $U_1(\beta)$ away from the central region for both terms is of the order $1/\beta^2$.

For real crystals showing small extinction effects the dynamical theory can be replaced by the kinematical theory. For this case $U_1(\beta)$ is the interference function in which the decay from the peak is the same as that of a Gaussian distribution. Generally, we shall consider $U_1(\beta)$ to be a delta function replaceable by a constant proportional to F^2, but the validity of this assumption rests upon the variance of $U_5(\beta)$ and $U_6(\beta)$. The kinematic theory can replace the dynamical theory if the crystal is a mosaic of smaller crystals. Since $U_5(\beta)$ and $U_6(\beta)$ are 'mosaic distributions', their variances must be relatively large if the small crystal blocks forming the mosaic aggregate are to be small enough for the diffraction pattern $U_1(\beta)$ to be approximated by a Gaussian distribution with narrow line width. This is true because a narrow mosaic distribution would imply that there was considerable extinction. Thus, if the crystal is ideally imperfect, the variances of $U_5(\beta)$ or $U_6(\beta)$ should be expected to be large. In other words, regardless of the state of crystal perfection, the convolution of $U_1 * U_5 * U_6(\beta)$ must exist over a considerable range.

For $U_2(\beta)$, the source intensity distribution, we have taken as a model

$$\begin{aligned} U_2(\beta) &= 1 - \tfrac{1}{2}\cosh\frac{1{\cdot}32\beta}{\beta_2} && |\beta| \le |\beta_2| \\ U_2(\beta) &= 0 && |\beta| \ge |\beta_2| \ . \end{aligned} \tag{3}$$

The analytic expression given in equation (3) agrees roughly with measurements we have made of the focus of our X-ray tubes, except that experimental source intensity distributions are not necessarily symmetric. β_2 is the half angle subtended at the crystal on the projected focus.

In considering the spectral distribution, we distinguish between the spectral distribution $V_3(\beta)$ passing through the X-ray tube window and the effective spectral distribution, $U_3(\beta)$, which is a modification of $V_3(\beta)$ effected by filtration, pulse amplitude discrimination and/or crystal monochromatization. $V_3(\beta)$ is the wavelength distribution of intensity available just outside the X-ray tube window (translated into the angle scale of the study crystal through Bragg's law); as such it includes the entire spectrum emitted by the tube including the white radiation as well as the characteristic lines (we neglect air path absorption). In Fig. 1(*a*) is shown approximately a typical spectrum on a wavelength scale from a Mo target tube incident on a study crystal. This distribution was generated at 50 kV using a single spherical topaz crystal in a linear 2:1 scan in which $d(\sin\theta)/dt$ was constant. The range of the scan in 2θ was from about 15 to 150° 2θ. (Unavoidably, a second order spectrum also appears.) The circular detector aperture used was approximately 0·9°. Full scale on the chart is 10% of the peak intensity of the $K\alpha_1$ line. A bland (nickel) filter was used to diminish counting losses due to nonlinearity. The spectrum shown is clearly not a 'pure' spectrum since aberrational components are present. Nevertheless, the essential nature of the spectral effect is apparent. In Fig. 1(*b*) is shown an approximate spectral distribution which was generated under the same conditions as in Fig. 1(*a*) except that a Zr filter and pulse amplitude discrimination (Parrish & Kohler, 1956) were used. Certain features should be noted. At the Zr edge the height of the profile is 2·3% of the $K\alpha_1$ peak intensity. The residual $K\beta$ line transmitted is 2·0% of the peak height. On the long-wavelength side the profile decays rather slowly. The profile extends over a range in wavelength in excess of 0·41 Å. If one integrates the portions of the profile exclusive of a narrow band within which the $K\alpha$ doublet is included, as suggested in the horizontal truncation procedure of Alexander & Smith (1962), one finds that 30% of the area under the profile is exterior to the characteristic $K\alpha$ lines. Also, as shown in Fig. 2, where the 2:1 scan of the 00*l* reflections obtained with Zr-filtered radiation is compared with the same scan taken with crystal monochromatized radiation, the effective range of the filtered spectrum is approximately 40 times the effective range of the crystal monochromatized spectrum. The 'background' shown in Fig. 2(*a*) (compared with Fig. 2(*b*), where the background is negligible) reveals several important facts: (1) The background, which is here primarily due to coherent scattering, is not uniform. (2) In viewing the 0,0,12 profile, one observes interference of this profile with the profiles due to 0,0,10, 0,0,14 and 0,0,16. Since the c lattice parameter is only of the order of 8·5 Å, Zr-filtered Mo radiation will not produce resolved lines. In fact, these interferences cannot be avoided except possibly for cells having lattice constants of 2·1 Å or less.

Since reflections overlap when filtered radiation is used, one must resort to arbitrary truncation procedures to attempt to isolate individual reflections. Such procedures must attempt to reject systematically the same portion of 'unwanted radiation' at all 2θ angles and must in practice also take into account the interaction of adjacent or neighboring reflections. An an-

alysis of systematic error is thus intractable since even larger errors are introduced by the unavoidable truncation procedures, however judiciously applied.

In Fig. 1(*c*) is shown approximately the spectral distribution incident on the study crystal when a monochromator is used. One effect of using the spectrum shown in Fig. 1(*c*) is virtually to eradicate background as shown in Fig. 2(*b*).

In our experimental work we have been using crystal monochromatized radiation almost exclusively for the last five years. We feel that the advantages of controlling the range of the spectral distribution in the incident beam in this manner are well worth the minimal extra effort required. We shall consider the effective spectral component $U_3(\beta)$ using crystal monochromatization in more detail in the next section, after proceeding with a description of the other aberrational components.

For spherical crystals we assume that the crystal size factor $U_4(\beta)$ is given by

$$U_4(\beta)=\sin^2\beta_4-\sin^2\beta \quad |\beta|\leq|\beta_4|$$
$$U_4(\beta)=0 \quad |\beta|\geq|\beta_4| . \qquad (4)$$

Here, β_4 is the half angle subtended from the crystal at the source. Implicit in equation (4) is the simplifying assumption of no vertical divergence.

In the mosaic structure model, Darwin (1922) distinguished between two types of disorder: (1) atoms are arranged in layers which deviate from planarity, and (2) the crystal is composed of an assemblage of smaller, ideal crystal blocks, each block slightly misoriented with respect to its neighboring blocks. In the category (1) can be included such anomalies as lattice distortion, dislocation edges, and strain. This disorder can be treated by a crystal model in which a set of dif-

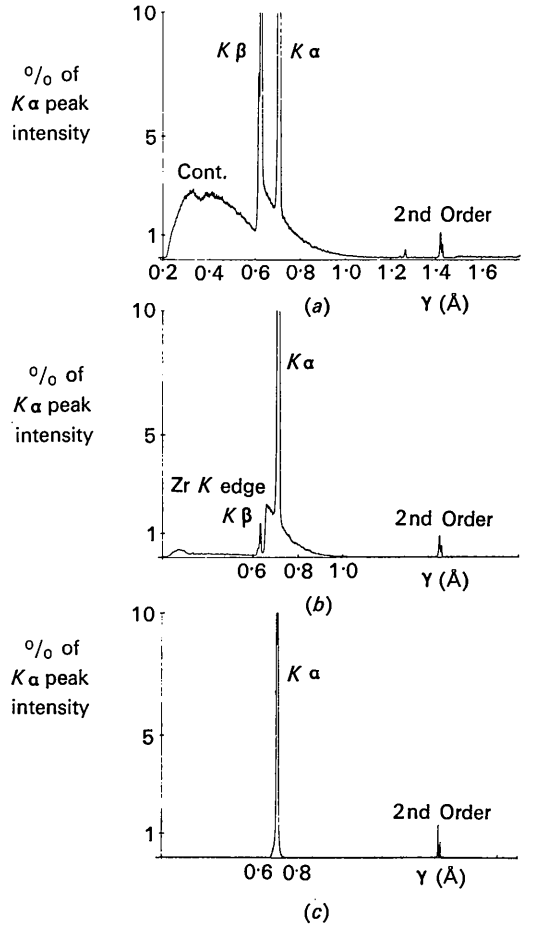

Fig. 1. Effective spectral distributions. Peak intensities are normalized at 100 %. (*a*) Profile generated when incident beam is 'normal' unfiltered Mo radiation. (*b*) Profile generated when Zr filter is used with pulse amplitude discrimination. Area above dotted line is only 70 % of the total area of the distribution. The effective spectral band pass, ignoring the obvious contribution of white radiation at low wavelengths, is greater than 0·4 Å. (*c*) Profile obtained using a (10$\bar{1}$) quartz monochromator. Background is negligible. Recorder time constant makes base width appear wider than the effective spectral band pass of 0·01 Å. (See Fig. 10).

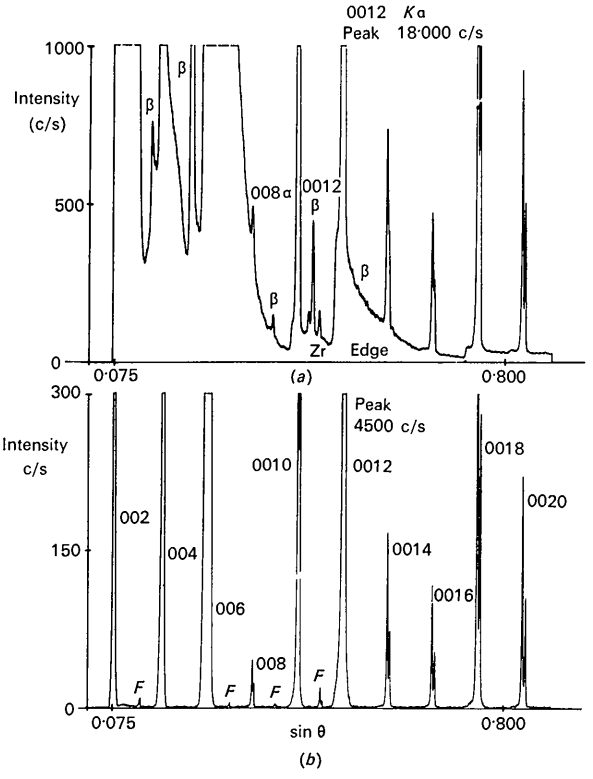

Fig. 2. Comparison of normal and crystal monochromatized radiation for the 00*l* spectra of topaz. 2:1 scan generated at $d(2\sin\theta)/dt=0{\cdot}03$ r.l.u. min^{-1} was used with target focus $8\times0{\cdot}4$ mm with a 3·5° angle of view. The topaz crystal diameter was 0·4 mm. (*a*) Incident beam was Zr-filtered Mo radiation. The signal-to-noise ratio measured adjacent to *Kα* peak of 0,0,12 reflection was 30:1. (*b*) Incident beam was (10$\bar{1}$) quartz monochromatized. The signal-to-noise ratio measured adjacent to the *Kα* peak of the 0,0,12 reflection was 1000:1. This high signal-to-noise ratio readily reveals forbidden reflections 003, 007, 009 and 0,0,11, designated by *F*.

fracting planes giving rise to a specific reflection is characterized as follows. The distance between successive planes is not constant, but varies statistically throughout the crystal. If $\bar{r}^*$ is the mean reciprocal spacing ($\bar{r}^* = 1/\bar{d}$), then $U_5(r^* - \bar{r}^*)\,\Delta r^*$ is the frequency of occurrence of parallel diffracting planes giving rise to the specific reflection for which the spacing deviates from the mean by $(r^* - \bar{r}^*)$. Since the same defect operates for higher orders of a given reflection, the distribution is dispersive. $U_5(\beta)$ is a 'strain broadening' aberration which gets larger with 2θ. In the reciprocal space picture $U_5(\beta)$ is represented as the extension of a point into a radial streak (see Fig. 8). In a prior paper (Ladell, 1961) we have assumed that $U_5(\beta)$ is a Gaussian distribution, but have not offered experimental evidence that this assumption is justified.

$U_6(\beta)$ is the angular distribution of crystal blocks forming a mosaic and is due to the second of Darwin's disorders. The reciprocal space picture of this distribution is the extension of a point in the reciprocal lattice to a spherical cap (see Fig. 7). Thus, both $U_5(\beta)$ and $U_6(\beta)$ have the effect of smearing an ideal reciprocal lattice point into an 'ellipsoidal' volume of concentrated central density. Although a Gaussian distribution is generally assumed, we have evidence (discussed below) that suggests this distribution may have appreciable Cauchy character for some crystals. For less imperfect crystals, as the distribution $U_6(\beta)$ becomes narrower, there must be an accompanying change in the dominating character of $U_1(\beta)$, as stated earlier. Whereas for crystals having a wide $U_6(\beta)$, $U_1(\beta)$ is dominated by the Gaussian character of the interference function; for crystals having $U_6(\beta)$ narrow, $U_1(\beta)$ is dominated by the slowly decaying Cauchy character of the intrinsic diffraction pattern. Thus, the convolution $U_1 * U_6(\beta)$ should theoretically converge to a Cauchy distribution rather than a delta function since transition from imperfect (large mosaic spread) to perfect (no mosaic spread) involves transition from the kinematical to the dynamical viewpoint. Therefore, the observed profile $U_0(\beta)$ should exhibit a slow decay, but it will be difficult to ascribe this slow decay to either $U_6(\beta)$ or $U_1(\beta)$ exclusively.

Intensity profiles for crystal-monochromatized radiation

The form of $U_0(\beta)$ for crystal monochromatized incident radiation is different from the case of nonmonochromatized radiation because of the angular dispersion introduced into the incident beam by the monochromator. Thus, in the nonmonochromatized case, all wavelengths are contained in all possible rays incident on the study crystal. In the monochromatized case, however, to a first approximation, to each direction of incidence on the study crystal there corresponds a specific wavelength. The degree of departure from this approximation is determined primarily by the diffraction properties of the monochromator crystal (rocking curve and dispersion) and secondarily by the source and study crystal distributions $U_2(\beta)$ and $U_4(\beta)$. We replace $U_2 * U_3 * U_4(\beta)$ in equation (1) by a new function $U_M(\beta)$, representing the radiation from the monochromator irradiating the study crystal, so that

$$U_0(\beta) = U_1 * U_M * U_5 * U_6(\beta)\,. \tag{5}$$

In deriving $U_M(\beta)$ we will consider the functions $V_i(\Lambda\beta)$, where

$$\Lambda = \frac{\tan\theta_M}{\tan\theta + \tan\theta_M} \tag{6}$$

and is introduced to allow for the dispersion of the monochromator crystal†. The functions $V_i(\Lambda\beta)$ are characteristic of the monochromator crystal in analogous manner as the functions $U_i(\beta)$ are characteristic of the study crystal: $V_1(\Lambda\beta)$ is the intrinsic diffraction pattern of the crystal monochromator; $V_3(\Lambda\beta)$ is the unmodified spectral distribution at the window of the X-ray tube, expressed on an angle scale; $V_5(\Lambda\beta)$ and $V_6(\Lambda\beta)$ are the radial and angular mosaic spread distributions respectively of the monochromator crystal. $V_2(\Lambda\beta)$ is the virtual source intensity distribution [equal to $U_2(-\Lambda\beta)$] and $V_4(\Lambda\beta)$ [$= U_4(\Lambda\beta)$] is the study crystal size distribution.

We consider first the dispersive components (those with index i odd) for point source and point study crystal. For these we may write

$$U'_M(\beta) = V_1 * V_3 * V_5(\Lambda\beta)\,. \tag{7}$$

The implications of equation (7) alter the simple geometric picture of the point source (perfect) monochromator and point study crystal in which only one unique wavelength can arrive at the point study crystal along a fixed path. For the more general case for which equation (7) applies, a distribution of wavelengths can traverse the same path from source to study crystal. To simplify the following discussion, we shall refer to the wavelength associated with $V_1(0)$, $V_3(0)$ and $V_5(0)$ (or the unique wavelength of the simpler case) as the 'central' wavelength.

Considering now (Fig. 3) the source distribution $V_2(\Lambda\beta)$, each point on the source sends toward the center of the study crystal (by virtue of the monochromator) a different 'central' wavelength. Thus, each 'central' wavelength incident on the center of the study crystal comes from one and only one point of the source. In producing the observable distribution $U_0(\beta)$, unlike the nonmonochromatized case, the source distribution $V_2(\Lambda\beta)$ is not convoluted with the distribution $U'_M(\beta)$, but operates as multiplier of $U'_M(\beta)$. Similar considerations apply to $V_4(\Lambda\beta)$. The combined effect of $V_2(\Lambda\beta)$ and $V_4(\Lambda\beta)$ then is to give rise to

$$\begin{aligned} U''_M(\beta) &= [V_2 * V_4(\Lambda\beta)]\,U'_M(\beta) \\ &= [V_2 * V_4(\Lambda\beta)]\,[V_1 * V_3 * V_5(\Lambda\beta)]\,. \end{aligned} \tag{8}$$

We refer to the function $[V_2 * V_4(\Lambda\beta)]$ as a 'stencil' function.

† Equation (6) assumes that the monochromator, study crystal and detector are arranged to develop and observe diffraction in the conventional anti-parallel position.

The significance of the stencil function is that it forces finite limits onto the spectral range incident on the study crystal.

We now consider the effect of the function $V_6(\Lambda\beta)$. Fig. 4 shows a ray diagram of a point source S, monochromator crystal, and point study crystal P. We neglect $V_1(\Lambda\beta)$ and $V_5(\Lambda\beta)$. When the monochromator is properly adjusted, a central ray of wavelength λ and intensity $V_3(0)$ proceeds along p, making an angle θ with the diffracting planes of the monochromator and is diffracted with intensity $V_3(0)\,V_1(0)$ through an angle 2θ along q toward the study crystal P. Due to the angular mosaicity function, $V_6(\sigma)$ of the monochromator crystal, another ray of wavelength λ' and intensity $V_3(\delta)$ can proceed along p' and be diffracted through $2\theta'$ along q' toward P. We wish to know the spectral distribution $W(\gamma)$ incident on P. For any wavelength the intensity arriving at P is given by $W(\gamma)=V_3(\delta)\,.\,V_6(\sigma)$, where δ and σ are deviations from the Bragg angle of the monochromator crystal. The following relationships among σ, δ, and γ are derived in Appendix A as equations (A17), (A14) and (A15),

$$\sigma_{\pm} = \tfrac{1}{2}\sin^{-1}\left\{\frac{q+p}{4a^2}\left[(q-p)\cos(\theta_M+2\delta)\right.\right.$$
$$\left.\left.\sin\theta_M \pm R\cos\theta_M\right]\right\} \qquad (9)$$

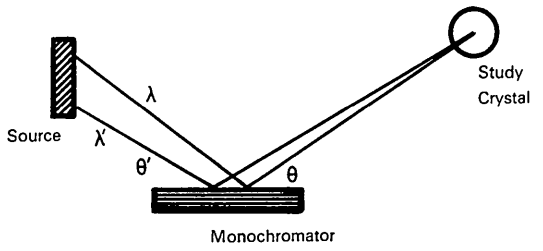

Fig. 3. Effect of monochromator on radiation incident on center of study crystal.

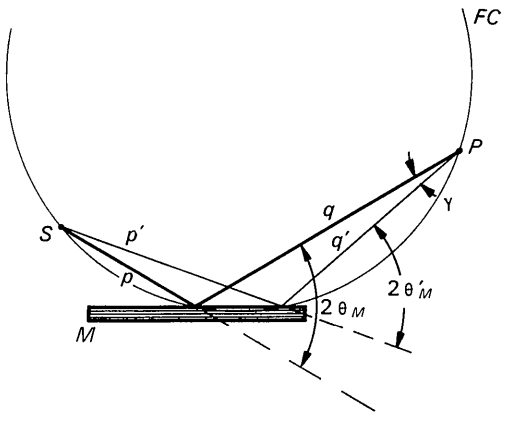

Fig. 4. Ray diagram for point source and study crystal with monochromator. S source; P study crystal; M monochromator; FC focusing circle; p, p' distances from S to point of reflection on monochromator surface; q,q' distances from P to point of reflection on monochromator surface; θ_M, θ_M' Bragg angles for monochromator crystal; γ angle between central ray and any other ray incident on P.

$$\gamma=(\sigma+\delta) \qquad (10)$$

where

$$R=\sqrt{4a^2-(p+q)^2\cos^2(\theta_M+2\delta)} \qquad (11)$$

and $2a$, the distance from S to P is given by

$$2a=\sqrt{p^2+q^2+2pq\cos 2\theta_M}\,. \qquad (12)$$

It should be noted that σ, and hence γ, is double valued: This means that the intensity distribution incident at P has two branches; *i.e.*

$$W(\gamma)=W_+(\gamma)+W_-(\gamma)=V_3(\delta)[V_6(\sigma_+)+V_6(\sigma_-)] \qquad (13)$$

where the $+$ and $-$ signs are associated with the choice of sign in equation (9). The dispersion in the two branches of $W(\gamma)$ is in opposite directions. The behavior of $W(\gamma)$ is discussed in detail in Appendix B. As shown in Appendix B, however, one of the branches of $W(\gamma)$ may be considered negligible for reasonable and judicious choices of the variables p and q and of $V_6(\sigma)$ and $V_3(\delta)$. We need therefore choose only the branch for which σ is given by equation (B5) or (B6) of Appendix B. Accordingly, the choice of sign indicator may be dropped and σ denoted by:

$$\sigma=\frac{1}{4a^2}\,\frac{p+q}{p-q}\,[(p+q)^2\cos^2\theta_M-(p-q)^2\sin^2\theta_M]\delta$$
$$=\Gamma\delta\,. \qquad (14)$$

Consider the study crystal at P. When the crystal is rotated, the incident distribution $W(\gamma)$ will be diffracted. As we have seen in the case where the mosaic spread $V_6(\sigma)$ was excluded, rotation of the study crystal involved a magnification factor Λ, given by equation (6). This magnification factor is merely the trigonometric factor which is derived in double crystal diffraction for the anti-parallel situation. For the case at hand, *i.e.* point crystal, point source and appreciable $V_6(\sigma)$, the different wavelengths converge on the point crystal. Accordingly, the magnification factor can no longer be derived on the basis of the anti-parallel geometry, in which convergence to the same point on the second crystal by different wavelengths from the same source point cannot occur. The appropriate correlation between the incident angular variable, γ, and the diffracted variable, β, is given by

$$\beta=-\gamma+\delta\,\frac{\tan\theta_M}{\tan\theta} \qquad (15)$$

where

$$\gamma=(1+\Gamma)\delta\,.$$

If we consider all the various component functions for the monochromator crystal, we finally arrive at a first order expression for $U_M(\beta)$:

$$U_M(\beta)=[V_2 * V_4(\Lambda\beta) * V'_6(\beta)][V_1 * V_3 * V_5(\Lambda\beta)] \qquad (16)$$

where

$$V'_6(\beta)=V_6(\sigma)=V_6\left(\frac{\beta\Gamma\tan\theta}{\tan\theta_M-(\Gamma+1)\tan\theta}\right). \qquad (17)$$

The most significant effect of crystal monochromatization is apparent from equation (16). Since both V_2 and $V_4(\Lambda\beta)$ are distributions which extend over finite (controllable) ranges, and since $V_6(\sigma)$ can also be controlled (Appendix A), the convolutions $V_2 * V_4(\Lambda\beta)$ and $V_2 * V_4(\Lambda\beta) * V'_6(\beta)$ extend over finite ranges. The distribution $V_2 * V_4(\Lambda\beta) * V'_6(\beta)$ 'stencils' the post factor $V_1 * V_3 * V_5(\Lambda\beta)$ (which is infinite in extension) and restricts the incident beam distribution to include only a finite (or truncated) spectral band pass.

If we assume that $V_1(\Lambda\beta)$ and $V_5(\Lambda\beta)$ are 'delta functions', the wavelength distribution in the beam interacting with the study crystal $U_M^{\lambda}(\lambda-\lambda_0)$ is given by

$$U_M^{\lambda}(\lambda-\lambda_0) = U_M(\delta)\frac{d\delta}{d\lambda} = \frac{V_3(\delta)\,[V_2 * V_4(\delta) * V_6(\Gamma\delta)]}{\lambda_0\,(\cot\theta_M\cos\delta - \sin\delta)} \tag{18}$$

where δ is the deviation of a given ray from the central ray reflected by the monochromator,

$$\lambda = \lambda_0\frac{\sin(\theta_M+\delta)}{\sin\theta_M}$$

and θ_M is the monochromator angle for which the principal wavelength of the central ray is λ_0. It should be noted that $U_M^{\lambda}(\lambda-\lambda_0)$ is not merely the wavelength distribution reflected by the monochromator, but is weighted by the available diffracting power distribution of the study crystal [because of $V_4(\delta)$]. Accordingly, $U_M^{\lambda}(\lambda-\lambda_0)$ is very much determined by the size and shape of the study crystal.

For narrow mosaic spread $V_6(\Gamma\delta)$, the *effective* spectral band pass is slightly greater than the range of the stencil function $V_2 * V_4(\delta)$. The width of the band pass can be made narrower by using a narrower focal source, smaller study crystal, or a monochromator of higher dispersion (smaller d spacing). A narrower focus is achievable by taking a smaller angle-of-view for a given focal dimension, or what is more effective, using a brighter focus of smaller focal dimensions. Using smaller study crystals and more dispersing monochromators, of course, causes a reduction in absolute intensity, but this is offset by an improved signal-to-noise ratio.

Fig. 5 shows the effects of altering the distribution $V_2(\delta)$ in the formation of the spectral band pass $U_M(\beta)$ in monochromatizing the $WL\beta_1$ line. In Fig. 5(*a*), the entire $L\beta$ spectrum is shown as generated in a 2:1 scan of an 0·5 mm diameter quartz study crystal, without using a monochromator. The abscissa has been converted to a wavelength scale, and the intensity ordinates are such that full scale represents 10% of the $L\beta_1$ peak. In Fig. 5(*b*), (*c*), and (*d*), a 10·1 quartz monochromator was used. In Fig. 5(*b*), the projected focal distribution was 1 mm wide, corresponding to an angle-of-view of 6°. In Fig. 5(*c*), the projected focal distribution was 0·5 mm wide, corresponding to an angle-of-view of 3°. In Fig. 5(*d*), the projected focal distribution was 0·1 mm wide, accomplished by using the line focus instead of the spot focus.

Because of the numerous characteristic lines in the $L\beta$ spectra [Fig. 5(*a*)] the theory presented above can be readily checked by monochromatizing in this region. Both at 3° and 6° angles-of-view the lines adjacent to the $L\beta_1$ are attenuated, the attenuation being more pronounced further away from the $L\beta_1$ line. For the 3° curve (obtained in a 2:1 scan at 101·2° 2θ), the effective

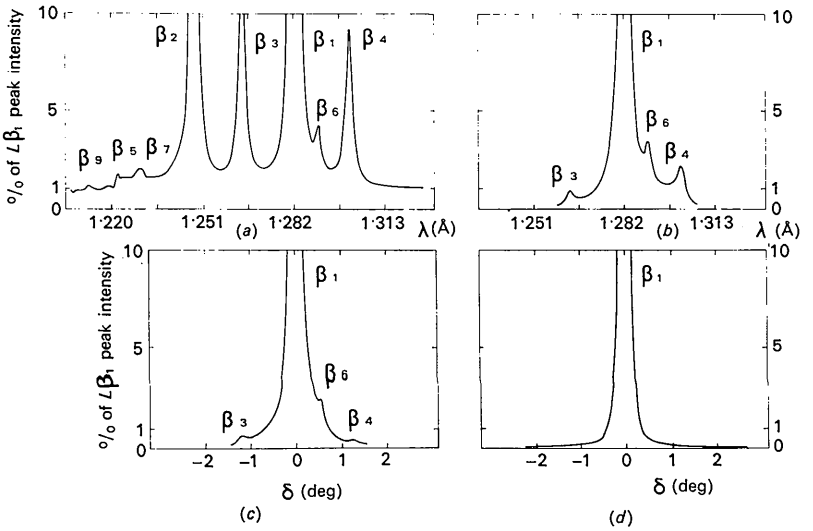

Fig. 5. Effectiveness of monochromatization in relation to projected focal dimension. Abscissae shown are on wavelength and angle scales. (*a*) $WL\beta$ spectra generated without monochromator. (*b*) $(10\bar{1})$ monochromator is used with 6° angle-of-view; projected focal dimension is 1 mm; study crystal diam. 0·5 mm. Strong $WL\beta_2$ line is effectively eliminated, but significant stumps of $L\beta_3$, $L\beta_6$ and $L\beta_4$ remain. (*c*) At 3° angle-of-view with projected focal dimension 0·5 mm further monochromatization is effected. $WL\beta_4$ is reduced to an almost negligible quantity. $WL\beta_3$ and $WL\beta_6$ are still seen, but with significant decrease in intensity. (*d*) Line focus is used with projected focal dimension 0·1 mm. All lines except the desired $WL\beta_1$ are completely eliminated.

band pass appears to be 0·052 Å. This value is more than the width that should be manifest in the absence of a mosaic spread component $V'_6(\beta)$. Thus, for the 3° angle-of-view the band pass should be somewhat greater than 0·037 Å and the experimental results confirm this, since the characteristic lines at the extreme ends of the profile are attenuated to such an extent that their presence is barely visible. In the 6° case the theory predicts the band pass should be greater than 0·073 Å. Although the $L\beta_4$ and $L\beta_3$ lines are attenuated by approximately a factor of 4, their readily observable presence indicates that the band pass is larger than the portion shown. The curve for the 6° angle-of-view demonstrates the necessity for spectral fiducial marks in determining the extent of the band pass. Unless we can extend the data for Fig. 5(*c*) to include regions where the $WL\beta_2$ and $WL\beta_5$ lines should be observed, we are unable to distinguish between a slowly varying coherently diffracted background (white radiation), which should be included as part of admitted spectrum, and the incoherently scattered background which must be excluded as already noted above. In Fig. 5(*d*), the neighboring lines are completely removed; but, of course, this has been accomplished at great loss of intensity.

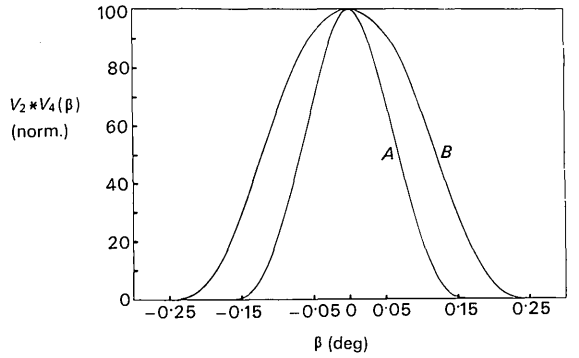

Fig. 6. Stencil function $V_2 * V_4(\beta)$ for the following experimental conditions: crystal diameter is 0·5 mm, virtual source to crystal distance is 175 mm and the focal spot dimensions are 10·0 × 1·6 mm. Curve *A* is calculated for an angle-of-view 3°, the case for Fig. 5(*c*). Curve *B* is calculated for an angle-of-view of 6°, the case for Fig. 5(*b*).

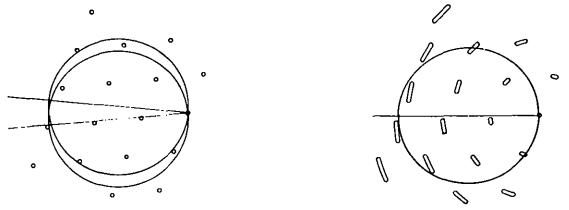

Fig. 7. Two representations showing role of nondispersive factors in Ewald construction. (See text.)

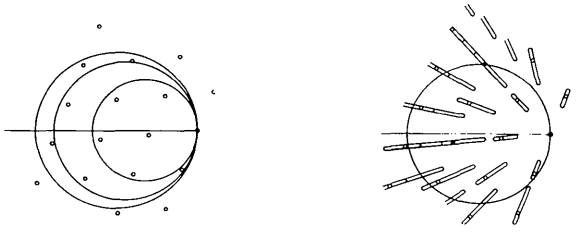

Fig. 8. Two representations showing role of dispersive factors in Ewald construction. (See text.)

Fig. 6 shows the assumed stencil functions $V_2 * V_4(\beta)$ operative for the cases shown in Fig. 5(*b*) and (*c*). These are based upon the models already discussed.

Systematic errors

While a description of the integrated intensity profile in terms of convolution theory is convenient for understanding the role of the various component interactions giving rise to the given observed profile, a much simpler description is desirable for graphic visualization particularly when one wishes to consider qualitatively the manner in which the component distributions cause superposition of adjacent profiles, a source of systematic error.

In Fig. 7 the role of nondispersive factors is shown in two representations. In the left-hand construction are shown two limiting circles of reflection and an array of points representing the reciprocal lattice of a crystal. The circles of reflection intersect at the origin of the reciprocal lattice and are displaced from each other by an angle which represents the angular range of nondispersive components such as the source and/or crystal range. Since the lunes are generated by circles of reflection which can be drawn for incident rays included within the limiting rays shown, all reciprocal lattice points included within the lunes are in reflecting positions. This same reflecting condition is shown by the construction at the right in Fig. 7. The construction at the right is formed by compressing the lunes into a single reflecting circle and extending the points into arcs equal to the angular divergence of the limiting incident rays of the construction at the left. The right-hand figure also is a representation which could be used to display angular mosaic spread. For this case the arcs are, of course, generated by an array of reciprocal lattice points for each of the crystal blocks which make up the crystal mosaic. The right-hand representation is a convenient condensation which shows the instantaneous reflecting conditions when nondispersive factors are operative.

In Fig. 8 equivalent representations of the role of dispersive factors are shown. The conventional construction is shown at the left. The inner circle of reflection represents the Ewald circle for the maximum incident wavelength and the outer circle represents the minimum incident wavelength.

The intermediate circle represents a characteristic wavelength. (The diagram is the familiar construction for Laue diffraction.) By changing the scale of the reciprocal lattice construction appropriate to each of

the circles included in the lune formed by the limiting inner and outer circles, one obtains the 'equivalent' construction shown at the right. Each point becomes a radial 'streak' (familiar in unfiltered precession diagrams).* The further the point is from the origin of the reciprocal lattice the longer is its streak. The right-hand representation applies not only to spectral band pass, but also to such dispersive factors as radial mosaic spread. The construction at the right shows overlap of these streaks; it is clear that the further the streaks from the origin, the greater the overlap. The overlapping of the streaks shows graphically interference of the type encountered when harmonics of a given radiation simultaneously satisfy Bragg's law. The extent of the radial streaks (or line segments) will be determined by the sum of the ranges of the individual dispersive components. As this sum becomes larger, the overlapping becomes greater and isolated streaks occur closer to the origin of reciprocal space and begin to overlap. The manifestation of such overlap is evident in Fig. 2(*a*) as was already discussed. The construction at the right in Fig. 8 shows how the resolution of diffraction lines from adjacent reflections is influenced by the extent of the range of the dispersive factors.

In Fig. 9 is shown the effect in reciprocal space of the combination of both the dispersive and nondispersive factors. In this diagram each point of the radial streaks has been extended into an arc. Here we see an overlap of a second kind. Whereas the irresolution evidenced by overlap of the first kind (Fig. 8) takes place at a distance from the origin and along radial lines, an enhancement of the irresolution occurs as evidenced by overlap in directions normal to the radial lines. One effect of the second kind of overlap is to bring the irresolution of adjacent reflections closer to the origin.

In considering the constructions of Figs. 7, 8 and 9 it is clear that the resolution of adjacent reflections is enhanced for a given reciprocal net for shorter spectral band passes. This is demonstrated in Fig. 10 which compares the observed diffraction in the vicinity of the 0,0,12 reflection of topaz under different spectral band pass conditions. To maintain the diffraction from 0,0,12 $K\alpha$ isolated from the neighboring 0,0,10 and 0,0,14 reflections, the profile must be restricted within the confines of the reciprocal lattice repeat which for the case cited is 0·2384 Å^{-1}. Fig. 10 shows that such restriction is not accomplished with either the direct beam (no filter) or a single filter. It is satisfied by the crystal monochromatized profile and also by the band pass which would be admitted through perfectly balanced Zr and Y filters.

* It has been correctly pointed out to us by J. Hornstra that in the case of crystal monochromatized radiation, anti-parallel arrangement, the radial streaks are not truly radial but take a direction such that the streak is inclined to the radial direction by the angle θ_M.

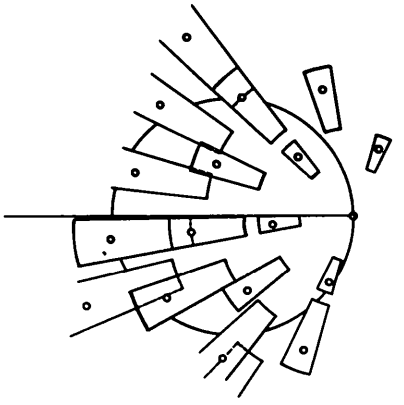

Fig. 9. Representation showing combined effect of both dispersive and nondispersive factors.

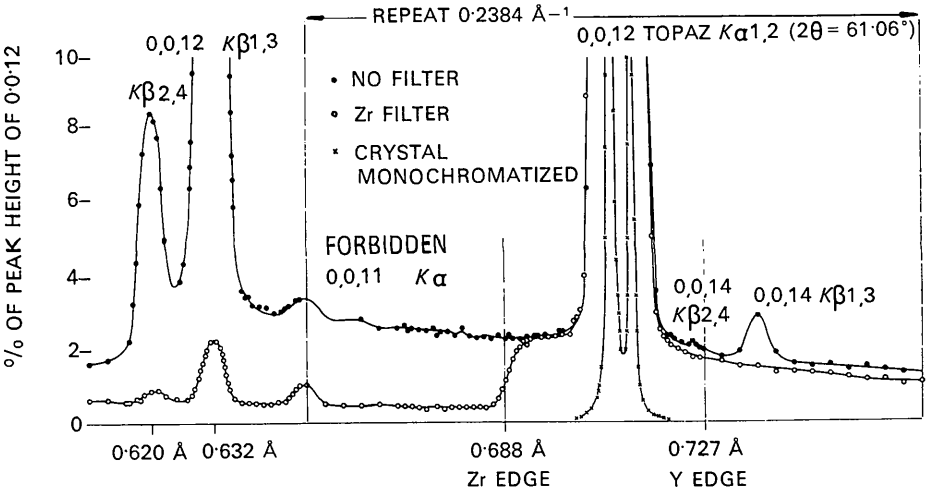

Fig. 10. Observed resolution in the vicinity of the 0,0,12 reflection of topaz for unfiltered, Zr-filtered and crystal monochromatized radiation. Curves obtained in 2:1 step scans. Abscissa shows equivalent wavelength scale.

Although the Zr–Y filters permit resolution of adjacent profiles at the 2θ angle cited, the resolution will not persist at higher 2θ angles where the streak defined by the separation of the absorption edges of Zr and Y becomes extended and eventually becomes longer than the repeat. It can easily be shown that resolution of adjacent reflections using the balanced filter pair Y–Zr with Mo radiation cannot be maintained over the complete 2θ range of crystals with unit-cell dimensions larger than 7·2 Å. Similarly, the resolution cannot be maintained over the complete 2θ range with the Ni–Co pair and Cu $K\alpha$ radiation for cell sizes exceeding 9·64 Å. The use of balanced filters is beset with other problems (Ladell, 1965). For techniques based upon their use the reader is referred to the work of Young (1963).

The superposition of overlapping reflections, as seen in the simplified representations of Figs. 7, 8, and 9, is a source of systematic error. Possible reduction or elimination of overlap is conditioned both by the ranges and form of the component distributions. In the remaining sections we consider these aspects of the problem.

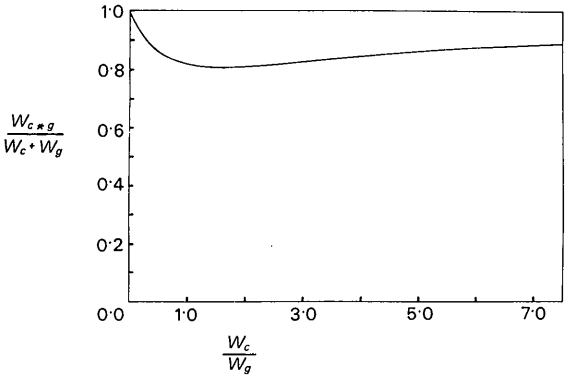

Fig. 11. Ratio of convolution line width to sum of component line widths as a function of ratio of component line widths. W_c is line width of Cauchy component, W_g is line width of Gaussian component and W_{c*g} is line width of convolution.

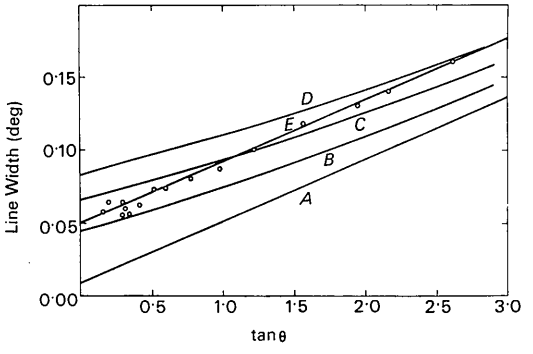

Fig. 12. Line widths for quartz study crystal. *A*: Calculated from two crystal spectrometer data. Line width of $WL\beta_1$, $\Delta\lambda = 0{\cdot}94$ X.U. *B*, *C*, *D*: Theoretical profile after convolution with Gaussian component with widths of 0·04°, 0·06° and 0·08° respectively. *E*: Theoretical profile after convolution of spectral profile with Cauchy component of width 0·042°. Observed data shown by open circles appear to agree with this case.

With $U_M(\beta)$ defined by equations (16) and (5), the observed profile using an incident beam of crystal monochromatized radiation is given by

$$U_0(\beta) = U_1 * U_M * U_5 * U_6(\beta) . \qquad (5)$$

The range of $U_0(\beta)$ is the sum of the ranges of the individual components; *i.e.*

$$2\beta_0 = 2[\beta_M + \beta_1 + \beta_5 + \beta_6] \qquad (19)$$

where β_M is the half-range of the spectral distribution diffracted from the study crystal,

$$\beta_M = \beta_2 + \beta_4 + \beta_6' \qquad (20)$$

where A, β_2, and β_4 have already been defined (Table 1) and β_6' is the half range of the distribution $V_6'(\beta)$, defined in equation (17). As pointed out in Appendix A, the range of σ (and consequently β_6') has a lower limit $\sigma_{\min}$ and a controllable upper limit. As is pointed out in Appendix B, the mosaic spread distribution $V_6(\sigma)$ for monochromator crystals normally used is such that the range σ_6 is narrower even than the formal limits. Accordingly, we will neglect this contribution to the range $2\beta_M$, and *a fortiori* to $2\beta_0$. The quantity $\beta_2+\beta_4$ is the range of angular divergence from the virtual source to the study crystal. The range β_0 is finite or infinite now depending only upon the ranges of the components U_1, U_5, and U_6. For the strain-free crystals such as topaz, quartz, silicon, or CaF_2 which we have been studying, we can assume both β_5 as well as β_1 to be effectively small. Thus, $U_0(\beta)$ of equation (5) is very well approximated by

$$U_0(\beta) = \text{constant } U_M * U_6(\beta) . \qquad (21)$$

Under these assumptions we have attempted to characterize $U_6(\beta)$. Since the stenciling of the spectral distribution does not significantly alter the central shape of the spectral profile, $U_0(\beta)$ as given by equation (21) represents (*a*) either the convolution of an essentially Cauchy distribution with a Gaussian distribution, or (*b*) a Cauchy with another Cauchy. A consequence of convolution theory is that the line width of the convolution of two or more Cauchy distributions is the sum of the line widths of the component distributions. A similar theorem applies for the squares of the line widths of Gaussian distributions in convolution. For mixed convolutions where the components are respectively Cauchy and Gaussian distributions, the line width of the convolution is less than the sum of the component line widths. We have calculated the ratio of the convolution line width, W_{c*g}, and the sum of the component line widths, $W_c + W_g$ as a function of the ratio of the component line widths W_c/W_g. The results are shown in Fig. 11. In Fig. 11 one observes that the convolution line width is narrowest when a Cauchy with line width 1·5 is convoluted with a Gaussian with line width 1·0.

In Fig. 12 the line widths of observed profiles for a quartz study crystal are plotted against tan θ. The angle scale spectral line width for $WL\beta_1$ (approximately the line width of U_M) as a function of tan θ for our

experimental conditions is shown as line A. The spectral line width used was based upon the work of Williams (Compton & Allison, 1935). The assumption that $U_6(\beta)$ is a Gaussian distribution leads to expected theoretical line widths according to the parametric lines B, C or D. The line of regression for the observed data, however, is line E which is parallel to line A. This constitutes suggestive evidence that $U_6(\beta)$ is a Cauchy distribution and is not accurately modeled by a Gaussian. Similar results are obtained when crystal monochromatized Mo $K\alpha$ radiation is used and line widths obtained for topaz are plotted against tan θ.

The distinction between the Cauchy or Gaussian model in the estimation of systematic error is shown in Fig. 13. In Fig. 13 the percentage area found by integration over a given range is plotted against the range in line widths for A, a Gaussian distribution; B, an infinite Cauchy distribution; and C, a truncated Cauchy distribution. The distribution C was truncated at 45 line widths, which is the experimentally observed spectral band pass at 138° 2θ for $U_M(\beta)$. Whereas virtually the entire area is included within 3 line widths for the Gaussian distribution, less than 98% is included within 30 line widths for the infinite Cauchy distribution. The truncated Cauchy gives intermediate results.

In Fig. 14 the systematic error expected for fixed ranges $\Delta\omega=2$, 3 and 4° based upon the assumption that the observed profile can be modeled upon an essentially truncated Cauchy distribution are shown. Thus, the maximum error in failing to scan the entire profile with a 2° scan is 4·2% at 150° 2θ. For a 4° scan the corresponding error is 1·5%, but there is no error in the 4° scan for the 2θ region under 100° 2θ. In all cases the errors, where they exist, are linear with tan θ. Since these depend upon the spectral band pass which can be narrowed experimentally, conditions can be imposed to diminish systematic error further.

Values shown in Fig. 14 should be acceptable only as indicators of the order of magnitude of systematic error because of the idealized component distributions assumed in the analysis.

Receiving apertures

Since both $U_6(\beta)$, a nondispersive component, and $U_M(\beta)$, a dispersive component, extend over large ranges, both distributions possessing appreciable Cauchy character, it is difficult to see how one set of minimum receiving apertures can be implemented in practice for either the ω or 2:1 scan for the entire 2θ range. In some instances it may be impractical to maintain minimum apertures large enough to accommodate the detection of the generated profile. Thus, for example, if $U_6(\beta)$ has a Cauchy component of line width 0·05° the contribution to the minimum receiving aperture $4\beta_6$ for 2:1 scanning needed for this component alone will be effectively 5·0° (since approximately 50 times the line width is required to accommodate 99% of the intensity). Similarly, large apertures will be required for ω scan techniques even for crystal monochromatized truncated Cauchy spectral distributions at high 2θ angles (see Alexander & Smith, 1962).

The constructions which were developed to show the systematic error which may arise from failure to resolve diffraction effects involving adjacent reciprocal lattice points are also useful for demonstrating some aspects of the role of receiving apertures used in conjunction with 2:1 and ω scan techniques. In Fig. 15 an isolated reflection is considered. Also, a succession of circles of reflection are shown. As the crystal is rotated, an arc of each successive circle encounters a different portion of the generalized reciprocal lattice point. The requisite aperture, assumed to be of constant size during the integrated intensity scan of the reflection, must be large enough to detect all the diffraction represented by the successive intersections of the circle of reflection and

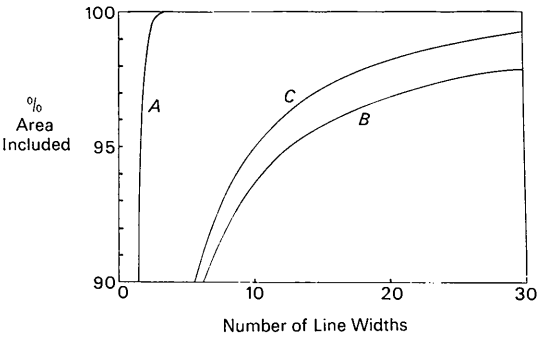

Fig. 13. Percentage of total area included within finite limits of integration. A Gaussian distribution. B Cauchy distribution. C Cauchy distribution truncated at 45 line widths.

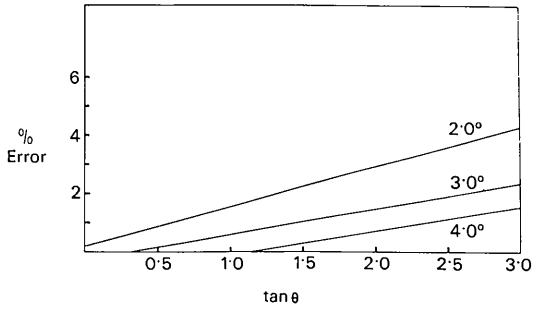

Fig. 14. Systematic error in integrated intensity due to definite range of scan as a function of tan θ for ranges of 2, 3 and 4° respectively. The observed profiles are assumed to be Cauchy distributions truncated at 45 line widths.

Fig. 15. Role of receiving aperture in scan of isolated reflection. Representation at left is for 2:1 scanning technique and representation at right is for ω scan.

generalized reciprocal lattice point. In the constructions of Fig. 15 the respective requisite apertures are shown by the heavily shaded arcs. In the 2:1 diagram (left figure) as the crystal is rotated, the detector also moves in 2:1 synchronization and accordingly the heavily shaded arcs progress away from the origin of the reciprocal lattice (up angle scan). The requisite size is determined by the nondispersive ranges, or the width of the generalized reciprocal lattice point. In the ω scan (right figure) the heavily shaded arcs are a constant distance from the origin of the reciprocal lattice. In this case the arc length, or requisite aperture, is determined by the dispersive components or the radial dimension of the generalized reciprocal lattice point.

Now it is clear that, for the case of an isolable reciprocal lattice point, the difference between the 2:1 and ω scan in terms of the diffraction or integrated intensity measured is only in the size of the aperture. Where the sum of ranges of dispersive components is equal to the sum of ranges of the nondispersive factors, the requisite apertures will be the same for both scan techniques. Such an equality can exist only at a specific 2θ angle. For lower 2θ angles, the requisite receiving aperture for the ω scan becomes less than that for the 2:1 and conversely the requisite aperture for the ω scan becomes larger for higher 2θ angles.

The use of crystal monochromatized radiation makes the dominant range that due to the nondispersive components since the principle dispersive factor, the spectral band pass, is minimized. Accordingly the ω scan technique for this case is the preferable technique, but only because this technique requires the smaller overall aperture except, of course, at extremely high 2θ values. As was previously noted the graphical descriptions shown in Figs. 7, 8, 9 and 15 are simplified. Reference to Table 1 shows that the ranges of $U_2(\beta)$ and $U_4(\beta)$, which are nondispersive components, contribute to the requisite receiving aperture for both scan techniques. Thus, the simplified discussion is only approximate. A more accurate graphical description can be developed with the use of the concept of a detecting volume (Spielberg & Ladell, 1960), but the complexity of such constructions obscures their interpretation.

It should be emphasized that the control of receiving apertures has no direct effect on the resolution of adjacent reflections where these are not resolved in the generated diffraction pattern as seen, for example, in Figs. 8 and 9.

Conclusions

Our work indicates that systematic error in intensity measurements can be significantly reduced by using crystal monochromatized radiation. Evaluation of systematic error for filtered radiation is intractable because of the large spectral band pass and the ambiguity of background determination; whereas in the monochromator case, both those factors are significantly reduced. There does not appear to be any primary advantage on the basis of which either a 2:1 or ω scan technique is to be preferred. Suggestive evidence exists to indicate that mosaic spread may be better modeled upon a Cauchy rather than a Gaussian distribution for certain types of crystals.

APPENDIX A
Monochromator geometry

To calculate the relationship between δ, σ and $A\beta$ introduced on page 109 (equations (9), (10) and (11); see also Fig. 4), we assume (Fig. 16) a Cartesian coordinate system in which the source S is placed at $(-a, 0)$ and the study crystal P at $(a, 0)$. The monochromator crystal lies along the line AB and the ray of wavelength λ passes along p, making an angle α with the x axis, and is reflected at R along the path q to intersect the x axis at $(a, 0)$ at an angle $(2\theta_M - \alpha)$. From simple trigonometry we find

$$\sin\alpha = \frac{q}{2a}\sin 2\theta_M \qquad (A1)$$

$$\cos\alpha = \frac{1}{2a}(p + q\cos 2\theta_M) \qquad (A2)$$

$$4a^2 = p^2 + q^2 + 2pq\cos 2\theta_M\,. \qquad (A3)$$

The coordinates of R are

$$(-a + p\cos\alpha,\ -p\sin\alpha)$$

or

$$\left(\frac{p^2-q^2}{4a},\quad \frac{-pq}{2a}\sin 2\theta_M\right).$$

The coordinates of A, the intersection of AB and the x axis, are

$$\left(-a - \frac{2ap}{q-p},\ 0\right).$$

Knowing the coordinates of A and R we find the equation of the line AB to be

$$[(q-p)\sin\theta_M]x + [(q+p)\cos\theta_M]y + (q+p)a\sin\theta_M = 0\,. \qquad (A4)$$

Consider an arbitrary point T on line AB. As already pointed out on page 109, radiation of wavelength λ' is reflected from T toward P. We may determine the corresponding value of $\theta'_M = \theta_M + \delta$ and the angular inclination of the crystal blocks of the mosaic diffracting at T by examination of the circle drawn through S, P and T. This circle has its center at $(0, c)$ on the y axis and radius $r = a/\sin 2\theta'_M$ (just as in the case of the Bragg–Brentano parafocusing condition). The equation of the circle is

$$x^2 + (y-c)^2 = a^2/\sin^2 2\theta'_M\,. \qquad (A5)$$

Since the circle must pass through $(\pm a, 0)$

$$c = a\cot 2\theta'_M\,. \qquad (A6)$$

A radius drawn from the center of the circle to T makes an angle 2η with the y axis. The effective normal to the block of the mosaic diffracting at T makes an

angle η with the y axis. From Fig. 16 we see that the coordinates of T are ($r \sin 2\eta$, $c - r\cos 2\eta$) or

$$\left[\frac{a \sin 2\eta}{\sin 2\theta'_M}, \quad \frac{a}{\sin 2\theta'_M}(\cos 2\theta'_M - \cos 2\eta)\right].$$

Substituting these coordinates into (A4) yields

$$\left.\begin{aligned}
\sin 2\eta = {} & \\
& \frac{1}{4a^2}[(p+q)(p-q)\cos(2\theta'_M-\theta_M)\sin\theta_M \\
& \pm (p+q)\cos\theta_M \times \\
& \sqrt{4a^2-(p+q)^2\cos^2(2\theta'_M-\theta_M)}] \\
\cos 2\eta = {} & \frac{1}{4a^2}[(p+q)^2\cos(2\theta'_M-\theta_M)\cos\theta_M \\
& \pm (q-p)\sin\theta_M \times \\
& \sqrt{4a^2-(p+q)^2\cos^2(2\theta'_M-\theta_M)}].
\end{aligned}\right\} \quad (A7)$$

To determine σ it is necessary to know the inclination of the normal of crystal blocks, not with respect to the y axis, but rather the inclination $(\eta - \eta_0)$ with respect to the normal to the crystal surface. We may determine η_0 by setting $\theta'_M = \theta_M$ in equation (A7), yielding

$$\left.\begin{aligned}
\sin 2\eta_0 &= \frac{1}{4a^2}(p^2-q^2)\sin 2\theta_M; \quad 0 \\
\cos 2\eta_0 &= \frac{1}{4a^2}[(p^2+q^2)\cos 2\theta_M + 2pq]; \quad 1
\end{aligned}\right\} \quad (A8)$$

$$\left.\begin{aligned}
\sin\eta_0 &= \frac{1}{2a}(p-q)\sin\theta_M; \quad 0 \\
\cos\eta_0 &= \frac{1}{2a}(p+q)\cos\theta_M; \quad 1.
\end{aligned}\right\} \quad (A9)$$

The second solutions in equations (A8) and (A9) may be rejected since they correspond to diffraction from that point of the crystal intercepted by the y axis.

Indeed, examination of Fig. 16 and equations (A7) shows that for each wavelength λ' there are two points on the crystal from which a properly oriented crystal block may reflect λ' to P. However, the value of $\sigma = \eta - \eta_0$ is different for the two points. There is, however, a value of λ' for which the two points degenerate to one point. This corresponds to the smallest $2\theta_M$ angle and wavelength which can be diffracted toward P. This angle, $2\theta'_{\min}$, can be obtained by equating to zero the radical in equation (A7) and noting that $2\theta'_{\min} = (2\theta'_{\min} - \theta_M) + \theta_M$ and $2\delta_{\min} = (2\theta'_{\min} - \theta_M) - \theta_M$:

$$\left.\begin{aligned}
\sin 2\theta'_{\min} = {} & \\
& \frac{2}{p+q}(a\sin\theta_M + \sqrt{qp}\sin\theta_M\cos\theta_M) \\
\sin 2\theta'_{\min} = {} & \frac{2}{p+q}(a\cos\theta_M - \sqrt{qp}\sin^2\theta_M)
\end{aligned}\right\} \quad (A10)$$

$$\left.\begin{aligned}
\sin 2\delta_{\min} = {} & \\
& -\frac{2}{p+q}(a\sin\theta_M - \sqrt{qp}\sin\theta_M\cos\theta_M) \\
\cos 2\delta_{\min} = {} & \frac{2}{p+q}(a\cos\theta_M + \sqrt{qp}\sin^2\theta_M).
\end{aligned}\right\} \quad (A11)$$

The corresponding values of η are

$$\left.\begin{aligned}
\sin 2\eta_{\min} &= \frac{p-q}{2a}\sin\theta_M \\
\cos 2\eta_{\min} &= \frac{p+q}{2a}\cos\theta_M
\end{aligned}\right\} \quad (A12)$$

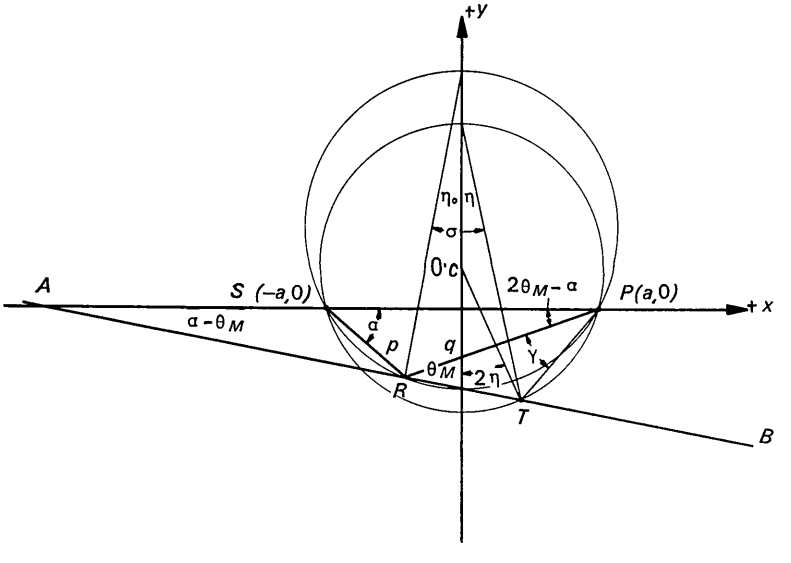

Fig. 16. Monochromator geometry.

$$\left.\begin{aligned}\sin\eta_{\min} &= \left(\frac{2a-(p+q)\cos\theta_M}{4a}\right)^{\frac{1}{2}}\\ \cos\eta_{\min} &= \left(\frac{2a+(p+q)\cos\theta_M}{4a}\right)^{\frac{1}{2}}.\end{aligned}\right\} \quad (A13)$$

A maximum value of wavelength which can be diffracted toward P is determined by limiting the divergence angle from S (Fig. 4). This will set a maximum value for η and hence for σ.

Substituting equations (*A*7) and (*A*8) into the identities $\sin 2\sigma = \sin 2\eta \cos 2\eta_0 - \cos 2\eta \sin 2\eta_0$, and $\cos 2\sigma = \cos 2\eta \cos 2\eta_0 + \sin 2\eta \sin 2\eta_0$, we find (noting that $2\theta'_M - \theta_M = \theta_M + 2\delta$):

$$\left.\begin{aligned}&\sin 2\sigma = \\ &\frac{q+p}{4a^2}[(q-p)\cos(\theta_M+2\delta)\sin\theta_M \pm R\cos\theta_M]\\ &\cos 2\sigma = \frac{1}{4a^2}[(p+q)^2\cos(\theta_M+2\delta)\cos\theta_M \pm \\ &\qquad R(p-q)\sin\theta_M].\end{aligned}\right\} \quad (A14)$$

where

$$R = \sqrt{4a^2-(p+q)^2\cos^2(\theta_M+2\delta)}\,. \quad (A15)$$

Setting $R=0$ again yields the value of $\sigma_{\min}$ corresponding to $\eta_{\min}$:

$$\left.\begin{aligned}\sin 2\sigma_{\min} &= \frac{q-p}{2a}\sin\theta_M\\ \cos 2\sigma_{\min} &= \frac{q+p}{2a}\cos\theta_M\,.\end{aligned}\right\} \quad (A16)$$

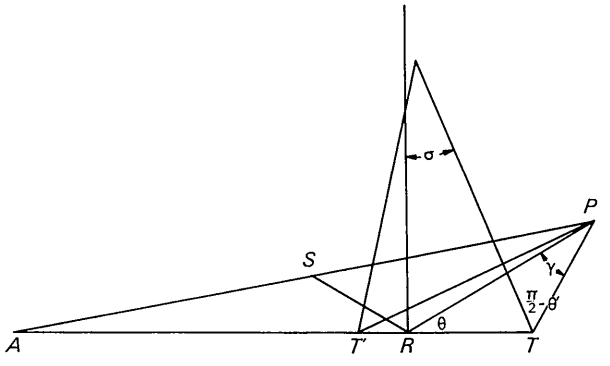

Fig. 17. Relationship between γ, σ and $\delta=\theta'-\theta$.

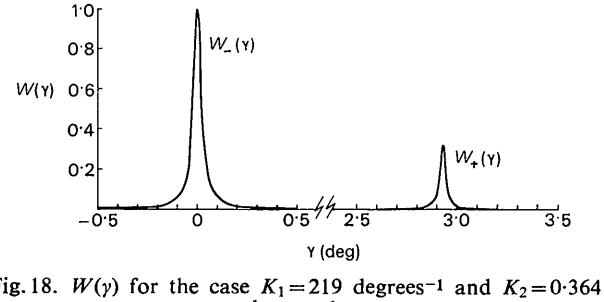

Fig. 18. $W(\gamma)$ for the case $K_1=219$ degrees^{-1} and $K_2=0{\cdot}364$ degrees^{-1}.

Comparison of equations (*A*9) and (*A*16) shows that $\sigma_{\min}=\frac{1}{2}\eta_0$.

The relationships between σ, δ, and $A\beta$ are seen in Fig. 17, where from the triangle RTP (positive value of σ),

$$\gamma = \pi-\theta_M-\left(\frac{\pi}{2}-\sigma+\frac{\pi}{2}-\theta'_M\right)=\sigma+\delta \quad (A17)$$

since $\theta'_M=\theta_M+\delta$.

APPENDIX B
Properties of W(γ)

As defined on page 109, the function $W(\gamma)=V_3(\delta).V_6(\sigma)$, where γ, σ and δ are related by equations (9) through (12). Since σ is double-valued, $W(\gamma)$ has two branches, $W_+(\gamma)$ and $W_-(\gamma)$ where $W_\pm(\gamma)=V_3(\delta)\,.\,V_6(\sigma_\pm)$. These two branches join (and σ is degenerate) for the value of $\delta=\delta_{\min}$ satisfying equation (*A*11) which, as pointed out in Appendix A, corresponds to the minimum wavelength reflected by the monochromator crystal to the point P in Figs. 4 and 16.

We may study the behavior of $W(\gamma\beta)$ by assuming certain models for $V_3(\delta)$ and $V_6(\sigma)$. We assume $V_3(\delta)$ to be Cauchy and $V_6(\sigma)$ to be either Cauchy or Gaussian; *i.e.*

$$V_3(\delta) = \frac{1}{1+K_1^2\delta^2} \quad (B1)$$

$$V_6(\sigma) = \exp(-K_2^2\sigma^2) \quad (B2)$$

or

$$V_6(\sigma) = \frac{1}{1+K_3^2\sigma^2}\,. \quad (B3)$$

If we assume that $V_6(\sigma)$ varies more slowly than $V_3(\delta)$, then $W(\gamma)$ will exhibit a maximum wherever $V_3(\delta)$ exhibits a maximum. From equation (*B*1) we see that this occurs when $\delta=0$. By inspection of Fig. 16, or of equation (*A*8), it is clear that the angular separation between the corresponding values of σ_+ and σ_- and hence of γ_+ and γ_-, equation (*A*15), is η_0, given by equation (*A*9).

From the data of Williams (Compton & Allison, 1935) for the width of the $WL\beta_1$ line, for a silicon (111) monochromator crystal, we find $K_1=219$ degrees^{-1}. If we assume $V_6(\sigma)$ to be Gaussian (equation *B*2) with a width 50 times greater than that of $V_3(\delta)$, $K_2=3{\cdot}64$ degrees^{-1}. (This would correspond to a monochromator rocking curve width of about 0·5°.) Typical values of p and q are 67 and 106 mm respectively. Under such circumstances, $\eta_0=2{\cdot}93°$, but $W_+(\gamma)$ is less than 1×10^{-5} throughout its range, and is therefore negligible. If $K_2=0{\cdot}364$ (rocking curve width 5°), $W_+(\gamma)$ attains a maximum value of 0·31. This case is plotted in Fig. 18 along with the appropriate curve for $W_-(\gamma)$. It should be noted that the spectral dispersions in the two branches of $W(\gamma)$ have opposite senses; *i.e.* $d\lambda/d(\gamma)$ is positive for $W_+(\gamma)$ and is negative for $W_-(\gamma)$. This can be seen by examination of Fig. 16, or by differentiating equation (*A*14) with respect to δ, and noting that $d\sigma/d\delta$ has the same sign as $d\lambda/d(\gamma)$.

Considering the possibility that $V_6(\sigma)$ is Cauchy (equation $B3$), if we assume a width of $V_6(\sigma)$ as much as 50 times greater than that of $V_3(\delta)$ ($K_3=4{\cdot}38$), the maximum value of $W_+(\gamma)$ is 6×10^{-3}.

We may simplify the equation ($A14$) for σ by making use of the approximations $\sin^{-1}x=x$ and $\cos(\theta_M+x) = \cos\theta_M - x\sin\theta_M$ for small values of x, and by neglecting terms involving x^2 *etc.* For the case $q>p$, we obtain

$$\sigma_+ = \frac{1}{4a^2}\frac{q+p}{q-p}\{[(q+p)^2\cos^2\theta_M+(q-p)^2\sin^2\theta_M]\delta+ (q-p)^2\sin\theta_M\cos\theta_M\} \quad (B4)$$

$$\sigma_- = \frac{1}{4a^2}\frac{q+p}{q-p}[(q+p)^2\cos^2\theta_M - (q-p)^2\sin^2\theta_M]\delta\,. \quad (B5)$$

For the case $q<p$, we obtain

$$\sigma_+ = \frac{1}{4a^2}\frac{p+q}{p-q}[(p+q)^2\cos^2\theta_M-(p-q)^2\sin^2\theta_M]\,\delta \quad (B6)$$

$$\sigma_- = \frac{1}{4a^2}\frac{p+q}{p-q}\{[(p+q)^2\cos^2\theta_M - (p-q)^2\sin^2\theta_M]\delta-(p-q)^2\sin\theta_M\cos\theta_M\}\,. \quad (B7)$$

For the case $q=p$

$$\sigma_\pm = \pm\sqrt{\tan\theta_M}\,\sqrt{\delta}\,. \quad (B8)$$

We have already demonstrated numerically that for the case $q>p$, the branch $W_+(\gamma)$ is usually negligible and hence the solution ($B4$) may be neglected. Similarly for the case $q<p$, $W_-(\gamma)$ is negligible and the solution ($B7$) may be neglected. Equations ($B5$) and ($B6$) are actually identical.

Only for the case $q=p$ do both branches of $W(\gamma)$ appear, and we may simply ignore this case by choosing q and p to be quite unequal in value.

It may be concluded that, except for rather pathological monochromator crystals, the curve $W(\gamma)$ has only one branch for a reasonable choice of the values of p and q.

References

ALEXANDER, L. E. & SMITH, G. S. (1962). *Acta Cryst.* **15**, 983.

ALEXANDER, L. E. & SMITH, G. S. (1964). *Acta Cryst.* **17**, 1195.

BURBANK, R. D. (1964). *Acta Cryst.* **17**, 434.

BURBANK, R. D. (1965). *Acta Cryst.* **18**, 88.

COMPTON, A. H. & ALLISON, S. K. (1935). *X-Rays in Theory and Experiment*. New York: Van Nostrand.

DARWIN, C. G. (1922). *Phil. Mag.* **43**, 800.

FURNAS, T. C. (1957). *Single Crystal Orienter Instruction Manual*. Milwaukee: General Electric Company.

LADELL, J. (1961). *Acta Cryst.* **14**, 47.

LADELL, J. (1965). Proceedings of A.C.A. Symposium at Suffern. *Trans. A.C.A.* **1**, 86.

LADELL, J. & SPIELBERG, N. (1963). *Acta Cryst.* **16**, 1057.

PARRISH, W. & KOHLER, T. R. (1956). *Rev. Sci. Instrum.* **27**, 795.

SPIELBERG, N. & LADELL, J. (1960). *J. Appl. Phys.* **31**, 1659.

YOUNG, R. A. (1963). *Z. Kristallogr.* **118**, 233.

ZACHARIASEN, W. (1945). *Theory of X-Ray Diffraction in Crystals*. New York: John Wiley.

Acta Cryst. (1966). **21**, 118

Twist-Korngrenzen und andere parakristalline Gitterstörungen in Polyäthylen-Einkristallen

VON R. HOSEMANN, W. WILKE UND F. J. BALTA CALLEJA*
Fritz-Haber-Institut der Max-Planck-Gesellschaft, Berlin, Deutschland

(*Eingegangen am* 26. *Juli* 1965 *und wiedereingereicht den* 29. *Oktober* 1965)

The analysis of equatorial small angle X-ray scattering of parallel oriented mats of polyethylene single crystals shows the existence of colloidal units with an average diameter of 300 Å in the lateral dimension. The line profile analysis of *hh*0 X-ray reflexions reveals that these structure units are mosaic blocks with paracrystalline distortions with $g=2\,\%$. Adjacent mosaic blocks must change their orientation by at least 0·6°, because otherwise they would scatter coherently. Black-field electron microscope moiré patterns of every two nearly parallel oriented single crystals obtained by other authors show straight lines with a trembling character, which can be explained by the size of the mosaic blocks and twist boundaries. The axis of disorientation is orthogonal to the chain direction. Average disorientations of 0·6–11° can explain both the moiré patterns and the X-ray diffraction photographs. The paracrystalline distortions within a single mosaic block are explained in terms of statistically distributed Reneker defects, $2n_{n+\delta}$-helices and damped thermoelastic waves.

Einleitung

Wenn zwei genügend dünne Kristalle um einen kleinen Winkel gegeneinander verdreht übereinanderliegen, kann man im Elektronenmikroskop Moirémuster beobachten. Solche Moirémuster wurden von mehreren Autoren (z.B. Agar, Frank & Keller, 1959; Fischer, 1963; Bassett, 1964; Holland, 1964) beobachtet. Die entsprechenden theoretischen Grundlagen sind in der Arbeit von Agar, Frank & Keller (1958) enthalten. Die Moirémuster von Polyäthyleneinkristallen erstrecken sich über Bereiche bis zu mehreren μ Aus-

* Gegenwärtige Anschrift: Centro de Investigaciones Fisicas, C.S.I.C., Madrid 6, Spanien.